

In-situ building halide-alloy dual-phase interfaces for dendrite-free sulfide solid-state batteries

Yao Liu^{1,2,3}, Jiamin Fu⁴, Mengzi Geng¹, Danni Wang¹, Shengjie Xia^{2,3}, Zhenlu, Yu¹, Yanyan Wang¹, Pushun Lu^{2,3}, Fanbin Zeng¹, Jie Shi¹, Changhong Wang^{2,3}, * , Xueliang Sun^{2,3}, * , Biao Zhang¹ *

¹*Department of Applied Physics, The Hong Kong Polytechnic University, Kowloon, Hong Kong 999077, China*

²*Eastern Institute for Advanced Study, Ningbo Institute of Digital Twin, Eastern Institute of Technology, Ningbo, 315200, China*

³*Zhejiang Key Laboratory of All-Solid-State Battery, Ningbo Key Laboratory of All-Solid-State Battery, Ningbo, 315200, China*

⁴*Department of Mechanical and Materials Engineering, University of Western Ontario, 1151 Richmond St., London, Ontario N6A 3K7, Canada*

Email: cwang@eitech.edu.cn; xsun@eitech.edu.cn; biao.ap.zhang@polyu.edu.hk

Abstract:

Argyrodite-type sulfide solid electrolytes are promising candidates for all-solid-state lithium-metal batteries due to their high Li-ion conductivity and favorable mechanical compliance. Nevertheless, their inherent chemical reactivity toward Li metal induces continuous interfacial degradation and filamentary Li growth, undermining their practical viability. Herein we engineer a surface-modified Li₆PS₅Cl electrolyte via co-treatment with GaCl₃ and InCl₃, enabling the in-situ formation of a multifunctional interphase upon contact with lithium metal. These conversion reactions produce a LiCl-rich, electronically insulating matrix interlaced with lithophilic Li-Ga and Li-In alloys. The LiCl matrix enhances interfacial energy to inhibit dendrite formation, while the alloy network promotes continuous and uniform lithium-ion transport. Concurrently, this interfacial layer scavenges irregular Li deposits formed during initial plating and acts as conformal interlayer to maintain intimate contact. Consequently, Li||Li symmetric cells achieve exceptional cycling stability (>2600 h at 0.5 mA cm⁻²). Paired with a Nickle-rich LiNi_{0.9}Mn_{0.05}Co_{0.05}O₂ cathode, full cells retain 80% capacity retention after 1700 cycles at 0.5C with ultra-thin 50 μm Li anode. This study highlights the effectiveness of engineered surface coating layers in stabilizing anode interface with minimal disruption to the sulfide electrolyte framework.

Introduction

Metallic lithium anodes are pivotal for next-generation high-energy-density batteries, offering an ultra-low redox potential (-3.04 V vs. Standard Hydrogen Electrode) and

exceptional theoretical capacity (3,860 mAh g⁻¹; 2,060 mAh cm⁻³).^[1] However, their reactivity with liquid electrolytes usually accelerates uncontrolled solid-electrolyte interphase (SEI) growth and raises safety concerns due to electrolyte flammability and lithium dendrite propagation.^[2-4] All-solid-state lithium-metal batteries (ASSLMBs) employing sulfide solid electrolytes (SEs) present a compelling solution.^[5] Sulfide SEs exhibit superior Li⁺ conductivity (>10⁻² S cm⁻¹) compared to other counterparts, such as oxides, polymers and borohydrides, mostly attributing to high sulfur polarizability and lowered Li⁺ migration barriers. Besides, the enhanced deformability arising from its low Young's module enables intimate anode/electrolyte interfacial contact.^[6, 7] Specifically, argyrodite-type Li₆PS₅Cl (651) demonstrates unique interfacial passivation behavior. Upon contact with lithium metal, 651 forms an interphase comprising Li₂S, Li₃P, and LiCl, which exhibits balanced ion conduction and electron blocking properties.^[8, 9] Despite the formation of a thermodynamically stabilized self-passivating interphase, 651-based ASSLMBs still face three critical challenges: (i) Electrochemical instability: The incompatibility of sulfide electrolytes with Li metal induces progressive interfacial degradation, elevating interfacial resistance during extended cycling; (ii) Mechanical degradation: repeated lithium plating/stripping generates interfacial voids and microcracks due to decomposition of SE and volumetric fluctuations of Li anode, promoting localized current concentration; (iii) Dendrite propagation: Grain-boundary-assisted lithium filament penetration is accelerated by residual electronic conductivity in the interphase and stress concentration at interfacial defects, culminating in short circuits.^[10-12]

To address the interfacial challenges of Li/651, extensive efforts have been taken to construct artificial buffer layers that segregate ion-conduction and electron-blocking functions.^[13-19] These typically employ compounds forming alloys and other self-limiting phases. For instance, the combination of lithiophobic LiH-Li₃N with lithiophilic LiMgLa multilayers is reported to suppress dendrite and reduce overpotential.^[20] Lithium alloy anodes, which have been widely investigated in traditional lithium batteries, usually offer high theoretical capacity, rapid ion diffusion (e.g., Li₃Mg, D_{Li+} ≈ 10⁻⁷ cm² s⁻¹), and improved sulfide electrolyte wettability.^[21-25] However, their substantial volume expansion (50-300%) induces mechanical stress in ASSLMBs, accelerating delamination or short-circuit. Extensive studies have been made to mitigate the problem.^[26-32] Building stratified composite Li-Al-Cl lithium alloy anode has been reported to form gradient distribution of Li₉Al₄ and LiCl, serving as SEI at surface while as skeleton in the bulk.^[33] Additionally, hybrid electrolyte architectures further demonstrate dendrite-suppression capability by scavenging the emerging dendrites before they fully penetrate the SE.^[34] Li_{0.388}Ta_{0.238}La_{0.475}Cl₃ (LTLC) with high current resistance was selected as intermediate layer inside 651, continuously consuming the penetrating Li filaments.^[35] Parallel approaches including intrinsic electrolyte modifications have also been widely explored, such as element doping at S and Cl sites by oxygen and other halogens.^[30, 36-41]

Despite these advances, the inherent trade-offs of the above interfacial engineering strategies have always been overlooked. Specifically, the formation of resistive interphase layers frequently compromises ionic conductivity, potentially accelerating

performance decay during extended cycling.^[42, 43] Thermomechanical mismatch between modified interfaces and adjacent components would cause progressive delamination and crack propagation under operational stress.^[44, 45] Furthermore, complex synthesis procedures required for multilayer architectures impose prohibitive cost barriers, fundamentally constraining the scalable deployment of ASSLMBs. Based on these, novel strategies are needed to ensure the benefits of interfacial modification without sacrificing other properties. Emerging lithium alloy and Li halide are favorable candidates as they demonstrate great compatibility with sulfide-based electrolytes.^[46] Herein, we engineer a sacrificial conversion layer through $\text{GaCl}_3/\text{InCl}_3$ (GI) surface modification of 651 particles. This multifunctional interphase operates via synergistic mechanisms. A lithophilic Li-Ga/Li-In alloy network and an electron-blocking LiCl matrix are simultaneously generated by a two-step in-situ conversion reaction. The percolating alloy phase establishes continuous ion pathways that spatially redistribute Li^+ flux, while the contiguous LiCl shell with high interfacial energy thermodynamically suppress dendrite nucleation. Notably, the modified SE delivers transformative enhancements in electrochemical performance. Critical current density (CCD) is increased by 100% to 2.2 mA cm^{-2} compared to pristine 651 (1.1 mA cm^{-2}). Li||Li symmetric cell demonstrates extended cyclability exceeding 2600 h at 0.5 mA cm^{-2} and around 800 h at 1.0 mA cm^{-2} . When integrated with $\text{LiNi}_{0.9}\text{Mn}_{0.05}\text{Co}_{0.05}\text{O}_2$ (Ni90) cathode, full cells exhibit exceptional cycle stability with capacity retention above 80% after 1700 cycles (0.5C) utilizing ultrathin 50 μm Li metal anode, corroborating successful inhibition of lithium dendrites during cycles. This interfacial engineering strategy concurrently addresses dendrite propagation, electrochemical degradation, and mechanical instability for fabricating durable sulfide-based ASSLMBs.

2. Results and Discussion

2.1 Sample preparation and structural characterization

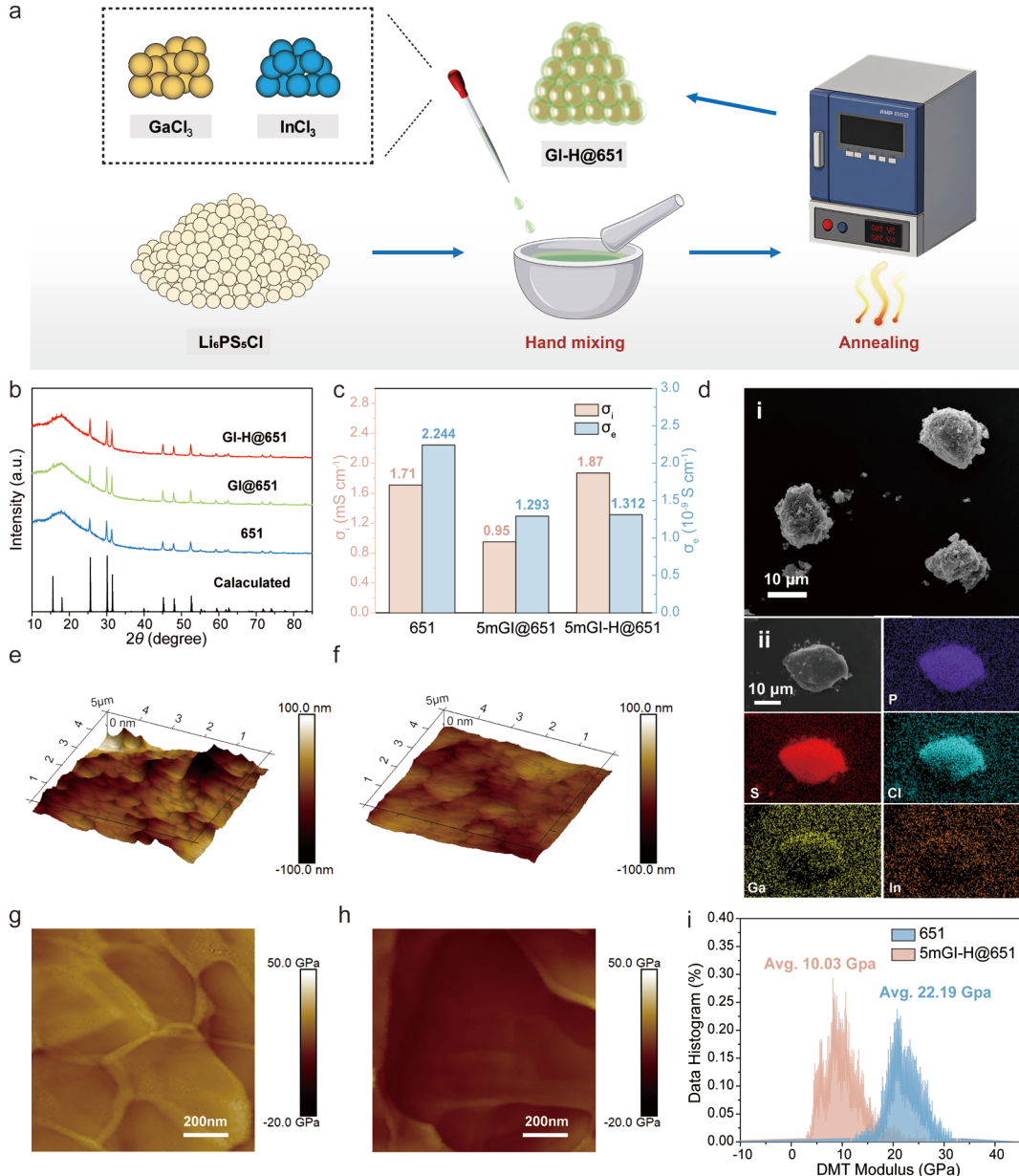


Fig.1 Preparation and characterization of SEs. (a) Schematic diagram of synthesizing GI coated 651. b) XRD patterns of 651, GI@651 and GI-H@651. c) Ionic conductivity and electronic conductivity of 651, 5mGI@651 and 5mGI-H@651. d) SEM and EDS mapping of 5mGI-H@651. The surface morphology of e) 651 pellet and f) 5mGI-H@651 pellet based on AFM analyses. Young's modulus distribution profiles of g) 651 pellet and h) 5mGI-H@651 pellet. i) Comparison of the average Young's modulus between 651 and 5mGI-H@651.

A solution-based treatment method is employed to realize the surface coating of GaCl_3 and InCl_3 on pristine 651 particles. Tetrahydrofuran (THF) is selected as the solvent for GI precursor solution for its low polarity and efficacy in dissolving metal halides.^[47] As

illustrated in Fig. 1a, 651 particles are thoroughly mixed with an fixed amount of GI-THF solution via mortar grinding, followed by annealing to ensure complete THF volatilization and enhance crystallinity. X-ray diffraction (XRD) analysis confirms that modified GI@651 particles retain the cubic argyrodite structure (F43m space group), which is identical to pristine 651 (Fig. 1b). The magnified spectrum (Fig. S1) demonstrates that annealing eliminates miscellaneous peaks. The modified particles are pelleted and implemented as an artificial interlayer between the SE and lithium metal anode. CCD tests are conducted to reveal the optimum concentration of GI for dendrites inhibition, and the same overall thickness is adopted for both SE with and without interlayer. The value of CCD rises continuously with the increased concentration of GI from 0.5 mmol, reaching the highest value of 1.9 mA cm^{-2} at 5 mmol and then dropping with higher GI concentration. The interlayer with 651 treated by 5 mmol GI is selected as the optimum configuration and marked as 5mGI@651 (Fig. S2-7). As mentioned before, post-annealing treatment is added to further enhance the performance by removing impurity phases, marked as 5mGI-H@651. The magnified comparison of CCD results of 651, 5mGI-651, 5mGI-H@651 is illustrated in Fig. S8. While 5mGI @651 shows higher overpotential compared to pristine 651, 5mGI-H@651 lowers the overpotential distinctly. Electrochemical impedance spectroscopy (EIS) in Fig. S9 quantifies the ionic conductivities of Li^+ ions (σ_{Li^+}) for 651, 5mGI@651, 5mGI-H@651 as 1.71, 0.95, 1.87 mS cm^{-1} , respectively. This restoration of ionic conductivity in the annealed sample demonstrates that the modification doesn't impair pristine advantage of 651. Additionally, chronoamperometry (CA) tests confirm pristine 651 particles possess the highest electronic conductivity (σ_e) of $2.24 \times 10^{-9} \text{ S cm}^{-1}$, posing a high risk of electron leakage inside anode interface. In comparison, both modified samples, i.e., 5mGI@651 and 5mGI-H@651, show lower value of σ_e , attributable to the insulating LiCl cladding layer formed during conversion reaction (Fig. 1c and Fig. S10).

Morphological evolution and elemental distribution of the modified particles are systematically characterized via scanning electron microscopy (SEM) coupled with energy-dispersive spectroscopy (EDS) mapping, as presented in Fig. 1d and Fig. S11-S12. Pristine 651 particles exhibit an average particle size of $\sim 3 \mu\text{m}$ with discrete morphology (Fig. S11). In contrast, 5mGI-H@651 particles display significant agglomeration after post-modification, forming larger secondary particles averaging $\sim 10 \mu\text{m}$ in diameter (Fig. 1d(i) and Fig. S12). This pronounced particle coarsening directly correlates with the surface coating and annealing treatment. Complementary EDS elemental mapping of 5mGI-H@651 (Fig. 1d(ii)) confirms homogeneous surface distribution of P, S, Cl, Ga and In. The absence of elemental segregation verifies conformal coating on the particle surfaces. Critically, the uniform spatial distribution of Ga and In signals verify their successful incorporation onto the particle surfaces without localized segregation. Atomic force microscopy (AFM) is further carried out to investigate the surface flatness and the mechanical properties of cold pressed pellets after attaching lithium metal. As shown in Fig. 1e and f, 651 pellet demonstrates higher roughness with small protrusions and pits, potentially inducing poor interfacial contact between SE and lithium anode.^[48, 49] Conversely, cold pressed 5mGI-H@651 pellet possesses a more compact and flatter surface attributed to the introduction of GI surface

coating. Fig. 1g-i presents the results of Young's modulus measurement of 651 and 5mGI-H@651 pellet peeling off from symmetric cells. The average value of 5mGI-H@651 (10.03 GPa) is significantly lower than 651 (22.19 GPa), consistent with a soft-shell@hard-core architecture when used as interlayer. The reduced Young's modulus of 5mGI-H@651 enhances the deformability under compression, enabling the formation of denser and more uniform interfaces. Simultaneously, this compliant interlayer would dynamically accommodate interfacial stress during battery operation, effectively compensating for contact loss to maintain persistent structural integrity.^[48]

2.2 Interface Stability of 5mGI-H@651 based Li Symmetric Cells

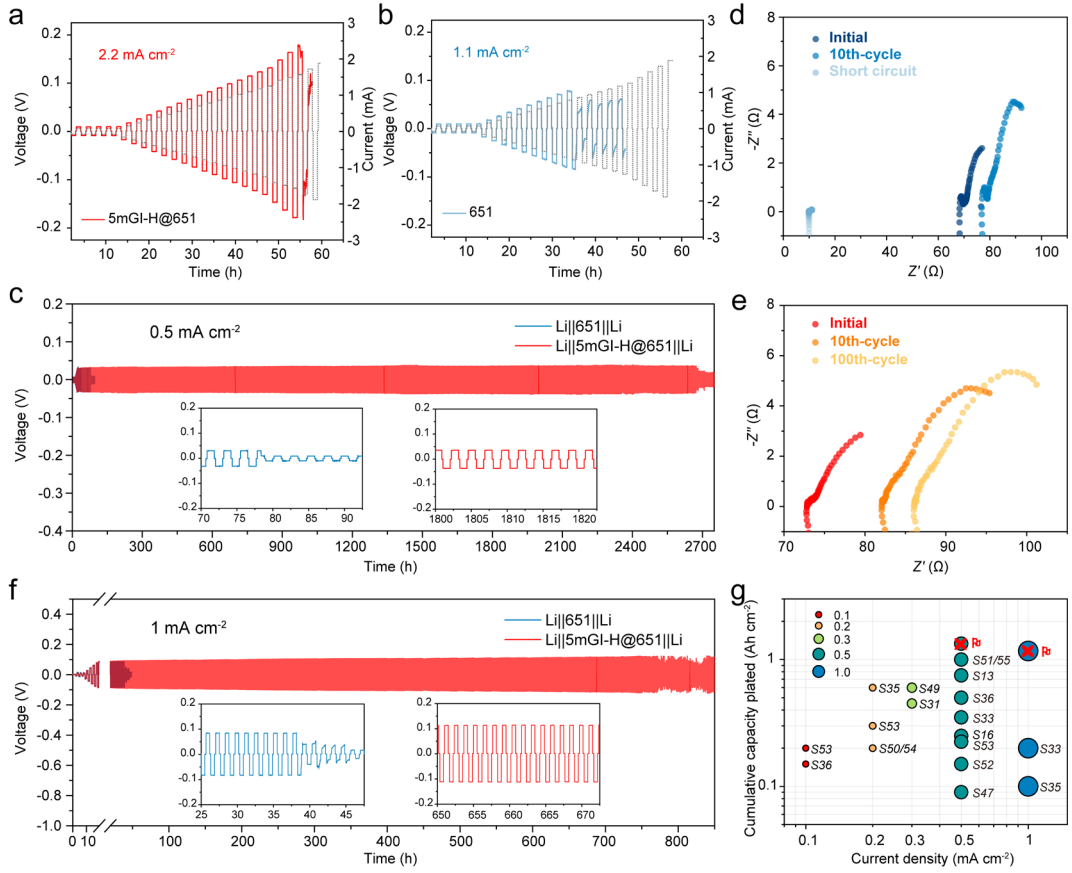


Fig.2 Electrochemical performance of symmetric cells. Galvanostatic cycling of Li-Li symmetric cells with a) 5mGI-H@651 and b) 651 at step-increased current densities. Voltage-time profiles of symmetric cells cycled under a constant current density and cut-off capacity of c) 0.5 mA cm^{-2} / 0.5 mAh cm^{-2} and d) 1 mA cm^{-2} / 0.5 mAh cm^{-2} . Evolution of Nyquist plots of symmetric cells cycled under 0.5 mA cm^{-2} / 0.5 mAh cm^{-2} utilizing e) 651 and f) 5mGI-H@651. g) Summary of reported Li-Li symmetric cell performances with 651 SEs.

To evaluate interfacial stability after introducing 5mGI-H@651, $\text{Li}||\text{Li}$ symmetric cells are fabricated utilizing 5mGI-H@651 as interlayer and with 651 as the bulk electrolyte, and the overall thickness is unified for comparison. CCD measurements, revealing the maximum sustained current of symmetric cells before voltage collapse induced by dendrite penetration, is employed by stepwise current increment of 0.1 mA cm^{-2} .^[36] As shown in Fig. 2a and b, the 5mGI-H@651 configuration achieves a maximum value of 2.2 mA cm^{-2} , doubling the value obtained by symmetric cell with pristine 651 (1.1 mA cm^{-2}). Long term cycling performance of symmetric cells at 0.5 mA cm^{-2} with the corresponding capacity of 0.5 mAh cm^{-2} exhibits stark contrasts as well. As shown in Fig. 2c, $\text{Li}||651||\text{Li}$ symmetric cell undergoes catastrophic short-circuit within 30 cycles and ends by an abrupt voltage collapse. The occurrence of the short circuit is also confirmed by the ex-situ EIS test shown in Fig. 2d, as the characteristic resistance of $\text{Li}||651||\text{Li}$ experienced a dramatic drop to 10Ω after 30 plating/stripping cycles.^[38] By contrast, the voltage profile in Fig. 2c presents exceptional long-term stability of nearly 2700 h for $\text{Li}||\text{5mGI-H@651}||\text{Li}$ symmetric cell with lower overpotential throughout

the whole cycling process. The corresponding EIS evolution in Fig. 2e further affirms the extraordinary interfacial integrity of Li||5mGI-H@651||Li symmetric cell, with merely marginal resistance growth observed after 100 cycles. Under higher current density of 1 mA cm⁻² and cut-off capacity of 0.5 mAh cm⁻², Li||5mGI-H@651||Li symmetric cell sustains nearly 800 hours of stable operation with relative constant overpotential prior to incipient soft short-circuit (Fig. 2f). In contrast, Li||651||Li cell fails to operate irreversibly within the initial 40 hours with a sudden voltage drop. To emphasize the long-term interfacial stability enabled by this design, we further benchmarks this work against the state-of-the-art 651-based symmetric cells as Fig. 2g.^[13, 16, 31, 33, 35, 36, 49-55]. Li||5mGI-H@651||Li symmetric cell delivers superior performance metrics in both current density and corresponding cumulative plated capacity.

2.3 The evolution of 5mGI-H@651 interlayer

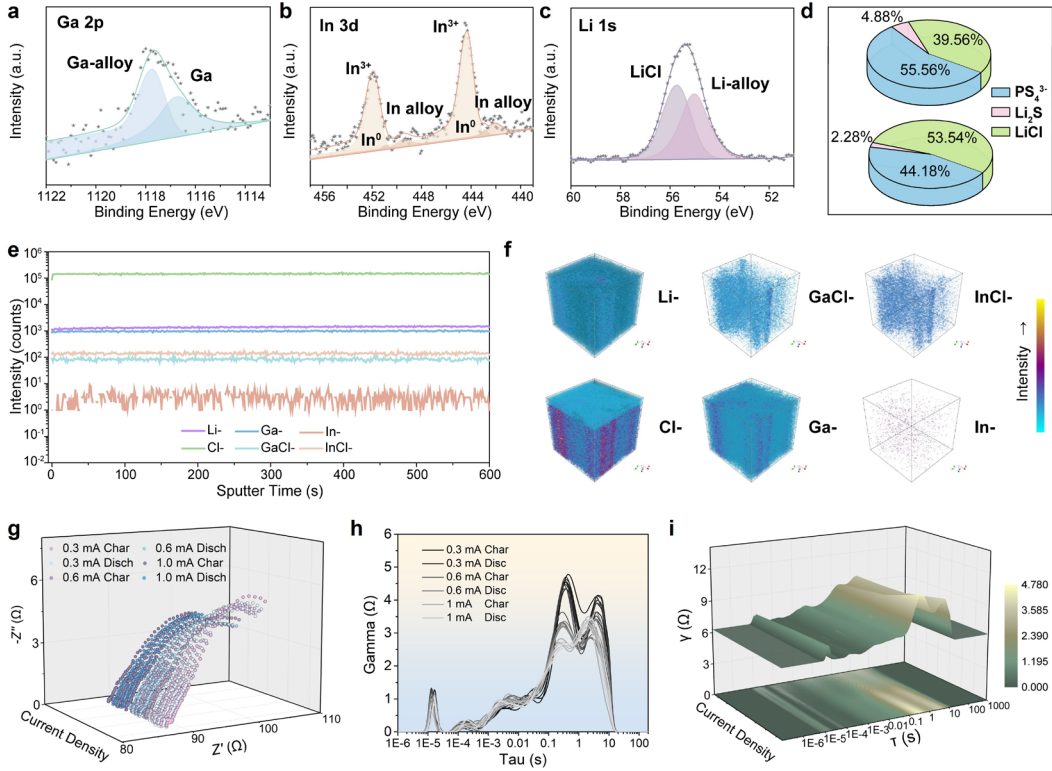


Fig.3 Interfacial evolution of the cycled interface. a) Ga 2p, b) In 3d and c) Li 1s XPS spectra and their fitting curves of the cycled Li/5mGI-H@651 interface for Li||Li symmetric cells. d) Semi-quantitative analyses of P, S, Cl species in anode interphases for Li||Li symmetric cells using 651 and 5mGI-H@651. e) TOF-SIMS depth profiles of various secondary ion species. f) 3D reconstruction of the Li^- , Cl^- , GaCl^- , InCl^- , Ga^- , and In^- secondary ion species based on the depth profiles obtained from the cycled Li/5mGI-H@651 interface for Li||Li symmetric cells. g) Potentiostatic Electrochemical Impedance Spectroscopy (PEIS) of Li/5mGI-H@651/Li symmetric cell cycling at various current densities. h) The corresponding DRT transformation result of (g). i) The corresponding 3D DRT transformation result of (g).

To elucidate the inner interfacial evolution of cycled interface, X-ray photoelectron spectroscopy (XPS) analysis is carried out for both Li||5mGI-H@651||Li and Li||651||Li symmetric cells (Fig. 3a-d and Fig. S13-S14). In the Ga 2p spectrum of cycled 5mGI-H@651 interface, the peaks of 1117.76 eV and 1116.74 eV are attributed to Li-Ga alloys and metallic Ga, respectively.^[17] The presence of these species indicates that GaCl_3 , coated on the surface of 651 particles undergoes a reductive reaction with lithium metal to first form elemental Ga, which subsequently reacts to generate Li-Ga alloys. Similarly, there are three distinct pairs of peaks found in In 3d spectrum. As shown in Fig. 3b, the peaks at 444.34 eV and 451.90 eV belong to In^{3+} from residual InCl_3 , peaks at 442.89 eV and 450.89 eV correspond to In^0 while peaks near 442.01 eV and 449.41 eV are assigned to Li-In alloy.^[55, 56] The presence of unreacted InCl_3 suggests that GaCl_3 preferentially reacts with lithium metal over InCl_3 , while the co-existence of In^0 and In alloy indicates that both the reduction of InCl_3 and the subsequent alloying with lithium occur concurrently. The Li 1s spectrum (Fig. 3c) features two dominant peaks:

one at 55.72 eV attributed to LiCl species formed by the reaction of interlayer with lithium metal. Another at 55.0 eV assigned to the emerging Li-alloy, aligning well with the previously discussed Ga and In spectra. The P, S, Cl spectra of both 651 SE and 5mGI-H@651 interlayer are presented in Fig.S13-14. The preservation of the PS_4^{3-} -tetrahedral framework is evidenced by peaks of P 2p (132.93/132.03 eV) and S 2p (162.91/161.72 eV). The distinct peaks observed at 160.53 eV and 161.63 eV correspond to Li_2S , a decomposition product formed upon direct contact with lithium metal.^[36, 57] Additionally, the presence of LiCl at the interface is verified by peaks at 200.54 eV and 198.88 eV in Cl 1s spectrum.^[17] Quantitative analysis of the relative peak areas for P 2p, S 2p and Cl 1s are employed to clarify the difference. As shown in Fig. 3d, the undesired decomposition product Li_2S demonstrates a significant reduction from 4.88% (651) to 2.28% (5mGI-H@651), while beneficial LiCl increases substantially from 39.56% (651) to 53.54% (5mGI-H@651).

In addition, time-of-flight secondary ion mass spectrometry (TOF-SIMS) is carried out to detect the compositional distribution at the cycled interface (Fig. 3e-f and Fig. S15-S18). As can be seen from the depth profiles shown in Fig. 3e, clear signals of Ga^- and In^- confirm the presence of Ga and In species during the interfacial reaction. The notably higher intensity of Ga^- relative to In^- indicates that GaCl_3 preferentially reacts with lithium metal before InCl_3 within the interlayer, corroborating the earlier XPS analysis. Signals of GaCl^- and InCl^- are attributed to the partially residual, unreacted GaCl_3 and InCl_3 precursors in the interlayer. The nearly constant intensity of these elemental signals throughout the entire 600-second sputtering period suggests a uniform distribution of these species within interlayer after reaction. Furthermore, 3D reconstructions of the six key fragments- Li^+ , GaCl^- , InCl^- , Cl^- , Ga^- and In^- are displayed, highlighting their critical roles in suppressing lithium dendrite within interlayer. As illustrated in Fig. 3f, these fragments are homogeneously distributed throughout the interlayer's 3D structure, forming a robust permeating network as an effective barrier against lithium dendrite growth.

The dynamic interfacial evolution of the interlayer during resting is investigated by tracking the in-situ EIS and corresponding distribution of relaxation times (DRT) of assembled symmetric cells.^[13] As shown in Fig. S19, impedance monitoring at 30-minute intervals captures an increase from 75.5Ω to 79Ω within the initial 90 minutes, signifying the activation reactions between introduced interlayer and lithium anode. This is followed by a gradual impedance rise over an extended resting period which eventually plateaued after 270 minutes, suggesting effective suppression of parasitic reactions via self-limiting interfacial processes.^[28] By transforming the EIS data from frequency to time-constant space, DRT decouples the simultaneous physicochemical processes operating within the multicomponent system.^[56] Fig. S20 present the DRT evolution of the symmetric cell, each relaxation time (τ) denotes a discrete electrochemical process. The peak centered at 10^{-5} s is attributed to the ongoing reaction between interlayer and Li metal, capturing the complex interfacial evolution involving electrolyte, Li metal, Li-alloy as well as transient intermediates.^[13] The gradually stable peak is ascribed to ion transport across the interfacial SEI (R_{int}), whereas the peaks at 10^{-2} ~ 10 s are highly reversible and correspond to charge transfer resistance (R_{ct}).^[56] To

further clarify the underlying interfacial evolution and assess potential soft-short circuits in the proposed interlayer, symmetric cells are subjected to cycling at stepwise current densities ($0.3 \rightarrow 0.6 \rightarrow 1.0 \text{ mA cm}^{-2}$) for 5 charge/discharge cycles, respectively, accompanied by in-situ EIS and corresponding DRT analysis (Fig. 3 g-i). The intensity of peaks located at 10^{-5} and within the $10^{-4} \sim 10^{-2}$ s (which are attributed to the chemical and mechanical contact resistance) remains stable throughout repeated plating/stripping cycles, indicating interfacial robustness under dynamic conditions. Interestingly, the previously merged peak observed in the $10^{-2} \sim 10$ s range during rest conditions evolves into two distinct peaks upon cycling. The newly emerged peak at $10^{-1} \sim 10^0$ s is ascribed to the interfacial resistance between alloy and electrolyte, while the one locates at $10^0 \sim 10$ is assigned to charge transfer resistance between Li metal and electrolyte. After over successive 1-hour plating/stripping cycles at increasing current densities ($0.3 \rightarrow 0.6 \rightarrow 1.0 \text{ mA cm}^{-2}$), both peaks exhibit progressively attenuated intensity, reflecting enhanced interfacial kinetics and improved transport. The observed improvements are attributed to the gradual formation of a stable SEI through repeated cycling. Notably, no additional relaxation features indicative of abnormal Li deposition or soft short circuits are observed during the entire cycling, affirming the integrity of the introduced interlayer. In conclusion, DRT analysis reveals 5mGI-H@651 interlayer could enable spatially homogeneous Li^+ flux distribution across the anode interface even under aggressive cycling conditions of high current densities and capacities.

2.4 Mechanism of lithium dendrite suppression by the interlayer

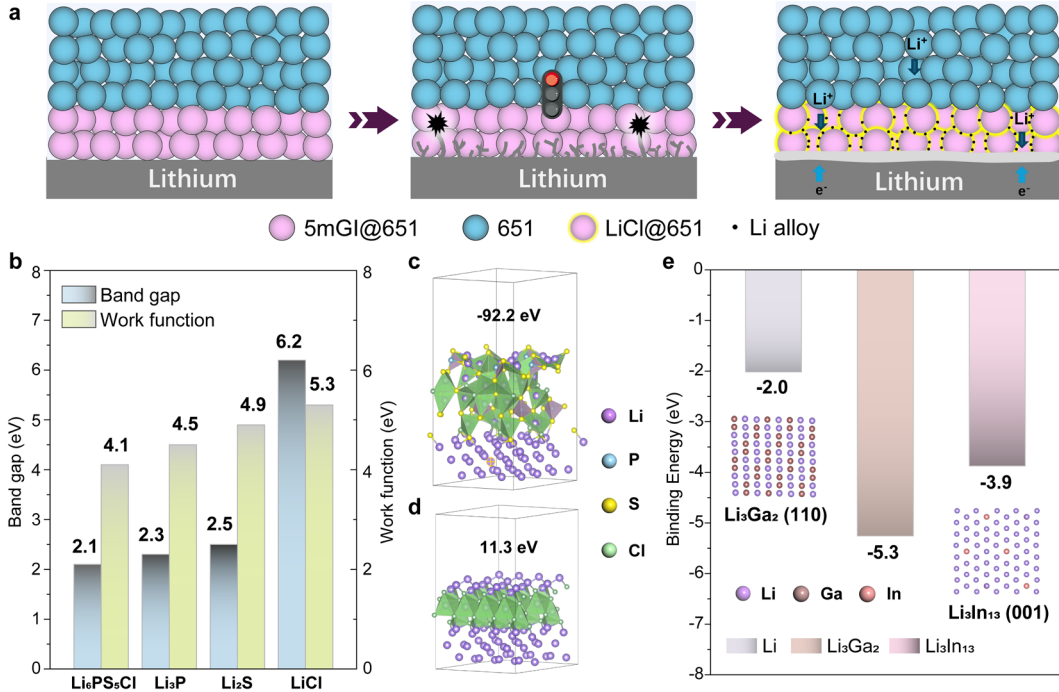


Fig.4 Mechanism of lithium dendrite suppression. a) Schematic diagram of the mechanism for lithium dendrite inhibition by the introduction of 5mGI-H@651 interlayer. b) The band gap and work function for LiCl , Li_3P , Li_2S and 651. The atomic structure of c) 651 (001)/Li (001) and d) LiCl (001)/Li (001) interface and calculation results of the interface energy. e) Binding energies of Li atom absorbed on Li (001) plane, Li_3Ga_2 (110) plane (c) $\text{Li}_{13}\text{In}_3$ (100) plane and relaxed Li/ Li_3Ga_2 (110) and Li/ $\text{Li}_{13}\text{In}_3$ (100) interface (inset). Color code: purple, Li atoms; blue, P atoms; yellow, S atoms; green, Cl atoms; brown, Ga atoms and pink, In atoms.

The underlying stabilization mechanism enabled by 5mGI-H@651 interlayer is schematically summarized in Figure 4a. Specifically, upon contact with lithium metal, 5mGI-H@651 particles undergo a thermally driven two-step conversion reaction (I: $\text{GaCl}_3/\text{InCl}_3 + \text{Li} \rightarrow \text{Ga/In} + \text{LiCl}$; II: $\text{Ga} + \text{Li} \rightarrow \text{Li-Ga alloy}$, $\text{In} + \text{Li} \rightarrow \text{Li-In alloy}$) to turn $\text{GaCl}_3/\text{InCl}_3$ coating into continuous LiCl shell with finely dispersed Li-Ga/Li-In alloys in the gaps between particles. In the early stage of plating, the conversion reaction consumes heterogeneous Li deposits, thereby conferring distinct advantage in curbing the propagation of lithium dendrites. Notably, the outside LiCl shell acts as an electron-blocking barrier with high interfacial energy to suppress parasitic side reactions and lithium nucleation, while the in-situ-formed Li-Ga and Li-In alloys possess higher binding energies towards Li^+ than pristine Li to eliminate ion aggregation and localized hot spots. The synergistic action of the insulating LiCl matrix and the lithiophilic alloy network therefore promotes the migration of lithium ions along the uniformly distributed channels, collectively mitigating parasitic reactions at Li/SE interface and dendrites growth into inner SE.^[18, 53, 58]

Density Functional Theory (DFT) calculations are carried out to provide quantitative validation for this stabilization mechanism. Fig. 4b compares the bandgap of 651 with three principal decomposition products (Li_3P , Li_2S , LiCl) at the anode

interface deduced from the density of state results. LiCl exhibits the widest bandgap of 6.20 eV, far exceeding Li₃P (2.3 eV), Li₂S (2.5 eV) and 651 (2.1 eV). Materials with bandgaps above 2.2 eV are generally regarded as wide gap semiconductors with promising electron-blocking capability.^[59] Notably, LiCl with wide gap of 6.20 eV are conducive to hinder electron tunneling between lithium metal anode and 651 SE to circumvent lithium dendrites. Complementary calculations of electronic work function reflects the minimum energy that electrons required to transport from a solid's interior to its surface, varying significantly depending on different electronic structure.^[59] LiCl exhibit the highest value of 5.3 eV over its counterpart Li₃P (4.5 eV), Li₂S (4.9 eV) and 651 (4.1 eV), confirming the minimum chance for parasitic electron leakage through the interlayer. We further examined the interfacial energy of representative LiCl in interlayer and pristine 651. SE with higher interfacial energy possesses inherent advantage for impeding Li nucleation within the SE as well as Li penetration even in porous structures.^[58] Fig. 4c and d demonstrate the scheme of the atomic structure of Li (001)/ 651 (001) and Li (001)/LiCl (001). The strongly negative value for Li (001)/ 651 (001) (-92.2 meV Å⁻²) implies the tendency for spontaneous chemical reactions between 651 and lithium metal, with the formation of unexpected decomposition products such as Li₃P and Li₂S. In sharp contrast, Li (001)/LiCl (001) in interlayer shows positive interface energy of 11.3 meV Å⁻², imposing a thermodynamic penalty on Li nucleation and penetration. Additionally, based on the calculation results of the crystal planes with lowest surface energy, we select Li (001), Li₃Ga₂ (110) and Li₁₃In₃ (100) as the basic substrates to investigate their binding energy with Li ions.^[17, 60] The interaction models of Li/Li (001), Li/Li₃Ga₂ (110), Li/Li₁₃In₃ (100) and their calculated binding energy are summarized as Fig. 4e. Li₃Ga₂ (110) and Li₁₃In₃ (100) exhibits the value of -5.3 eV and -3.9 eV, respectively, both substantially exceeding the value of -2.0 eV for metallic Li (001). The pronounced enhancement in adsorption directly correlates with superior lithiophilicity of Li₃Ga₂ and Li₁₃In₃. Such strong affinity towards Li ion confers distinct advantage in creating percolating Li⁺ diffusion channels and directing spatially uniform Li⁺ flux for dendrite-free plating.^[61] Collectively, the synergistic interphase stabilization mechanism delineated by previous characterization and electrochemical tests is here quantitatively corroborated by three key factors: (1) wide band gap and high work function conferring LiCl with exceptional electronic insulation; (2) dendrite-repelling positive interfacial energy of LiCl with lithium metal; (3) strong Li-ion affinity of Li-Ga and Li-In alloy phases.

2.5 Electrochemical performance of NCM/Li Cells with 5mGI-H@651 interlayer

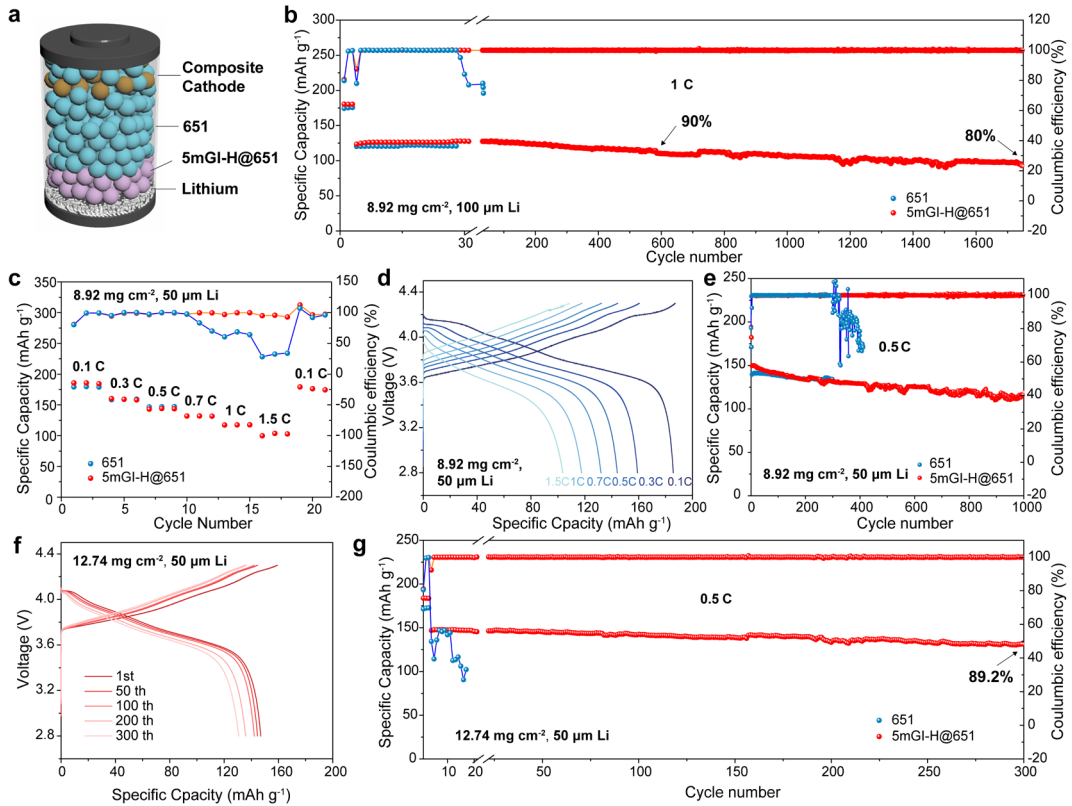


Fig.5 Electrochemical performance of full cells coupled with a Ni90 cathode. a) Diagram of assembled Li/5mGI-H@651/Ni90 full cells. Active material loading of 8.92 mg cm⁻²; b) Long-term cycling stability of full cells at 1 C. c) Rate capability and d) Charge/discharge curves of full cells (ultra-thin 50 μm lithium anode). e) Long-term cycling stability of full cells at 0.5 C (ultra-thin 50 μm lithium anode). Active material loading of 12.74 mg cm⁻²; f) Charge/discharge curves and g) Long-term cycling stability of full cells at 0.5 C (ultra-thin 50 μm lithium anode).

To validate practical viability of the introduced interlayer, ASSLMBs are configured with Ni90 composite cathode. 20 mg 5mGI-H@651 interlayer is positioned between Li metal anode and 60 mg 651 electrolyte (Fig. 5a). Fig. S21 displays enhanced discharge capacity (209.3 mAh g⁻¹) and initial coulombic efficiency (86.3%) for the cell with 5mGI-H@651 at 0.02C with 8.92 mg cm⁻² active material loading, in contrast to 195 mAh g⁻¹ and 84.0% for the cell using 80 mg 651 only. With 100 μm lithium anode, 5mGI-H@651 full cell demonstrates stable charging and discharging cycles with superior capacity retention of over 90% within 580 cycles and capacity retention above 80% for over 1700 cycles. While the 651 cell short-circuits after only 40 cycles. (Fig. 5b) Under the harsher testing conditions of 50 μm ultra-thin lithium anode, the cell with pure 651 SE encounters short-circuit as the current density rises to 0.7C, with the corresponding coulombic efficiency starts to drop quickly. While 5mGI-H@651 full cell retains exceptional rate capability with remarkable high discharge specific capacity of 103.7 mAh g⁻¹ even at a high current density of 1.5C. Especially, the specific capacity recovers to the original level as the current density returns to 0.1C, implying great reversibility of lithium-ion transport (Fig. 5c). Fig. 5d illustrates the fine-maintained

galvanostatic charge-discharge curves of 5mGI-H@651 full cell. Relatively low polarization can be observed for various current densities with considerable specific capacities, further attesting its interfacial stability within the voltage window of 2.8-4.3 V (vs Li⁺/Li). Long-term cycling is investigated also for the circumstances of 50 μm ultra-thin lithium anode. 5mGI-H@651 full cell still displays more stable cycling stability against full cell with only 651, with capacity retention of 79.7% around 1000 cycles at 0.5 C and capacity retention of over 98.0% around 80 cycles at 1C (Fig. 5e and S22). To advance toward higher energy densities in ASSLMBs, elevated active material loading of 12.74 mg cm⁻² is implemented. Fig. S23 demonstrates the rate capability from 0.1C to 1C, where 5mGI-H@651 full cell maintains stable charge discharge cycling. Concurrently, 651 full cell suffers catastrophic short circuits at 0.8C due to the rapid interfacial degradation. Cycling capability at 0.5C further validates the superiority of 5mGI-H@651 full cell, exhibiting 89.2% capacity retention with high coulombic efficiency of 99.9% over 300 cycles. (Fig. 5f and g) The galvanostatic charge-discharge curves indicate minimal capacity decay throughout cycling, while 651 full cell fails to function under identical conditions. Extending active material loading to ultra-high value of 32.48 mg cm⁻² (composite cathode pellet), full cell utilizing 5mGI-H@651 interlayer preserves notable capability within 1C (Fig. S24). Fig. S25 further reveals exceptional stability as the cut-off charge voltage extends to 4.7 V (8.92 mg cm⁻² active material loading), indicating that the introduction of interlayer doesn't sacrifice oxidation stability. The absence of interfacial deterioration or adverse reactions underscores the system's immense potential for high-energy-density ASSLMBs.

3. Conclusion

In summary, we engineered a novel interlayer through GI surface modification of 651 particles, effectively mitigating dendrite propagation in argyrodite-based ASSLMBs. The in-situ formed multifunctional interphase comprises a continuous LiCl-rich electron blocking matrix interlaced with lithiophilic Li-Ga/Li-In alloys, originating from a two-step conversion mechanism upon lithium contact. This architecture concurrently delivers critical functionalities electrochemically, chemically and physically, including thermodynamic dendrite suppression via LiCl's high interfacial energy, homogeneous Li⁺ transport through percolating alloy networks, early-stage dendrite scavenging through preferential consumption of irregular lithium and maintained intimate contact by the deformable conformal interlayer. Consequently, the fabricated Li||Li symmetric cells achieve exceptional long-term cycling performance of more than 2600 h under 0.5 mA cm⁻². With 50 μm ultra-thin Li anodes, Full cells utilizing Ni90 composite cathode retain 80% capacity retention after 1700 cycles at 0.5 C. This work presents a strategic approach to leveraging surface-engineered SE as interlayer, effectively stabilizing the anode interface while preserving the intrinsic characteristics of pristine SE for advancing practical ASSLMBs.

4. Experimental Section

Materials Synthesis: 651 was purchased from China Automotive Battery Research Institute Co., Ltd. GaCl₃ (>98.0%, Aladdin) and InCl₃ (99.995%, Macklin) was dissolved into 1 ml THF with different concentrations. Then 400 μL GI-THF solution and 200 mg 651 particles were mixed and hand grounded to form uniform slurry. The slurry was dried under vacuum followed by cold pressing as pellet. The coated GI@651 was further annealed at 180 °C for 5h to obtain GI-H@651.

Cell assembly: For Li/SE/Li symmetric cells, 100 mg 651 was poured into a hollow cylinder mold and pressed at 2T to make a pellet. Two pieces of Li metal (with diameter of 10 mm) were attached onto both sides of the pellet SE. For Li/SE/Li symmetric cells with interlayer, 60 mg 651 was pelleted first as the same procedure, then 20 mg 5mGI-H@651 was added onto both sides of the SE pellet followed by the attach of two Li metal. The Ni90 composite cathode was prepared by mixing Ni90, 651 SE and vapor grown carbon fiber (VGCF) with mass loading of 70:27:3. 651 SE was added to the Ni90 cathode (180 mAh g⁻¹) to construct a good ion-conduction network. For Li/SE/Ni90 full cells, a total of 80 mg SE was poured into a hollow cylinder mold and pressed at 2T to make a pellet. Then Ni90 composite cathode with different mass loading was spread evenly over the SE and pressed by 5T for 5min. Finally, lithium metal with different thickness was placed on another side of the SE pellet.

Electrochemical Performance Tests: The ionic and electronic conductivity of SEs were determined as follows. First, 80mg 651 particles were cold pressed into a pellet under 4T. Then, two stainless steel rods were used as the blocking electrodes. Ionic conductivity of the SE was calculated from the EIS measuring result of the bulk resistance using a Biologic VMP-3 electrochemical workstation, with a frequency range of 10⁶ to 100 mHz and an alternating current voltage amplitude of 10 mV. Electronic

conductivity of the SE was determined using direct current polarization method with applied voltage of 0.1 V, 0.2 V, 0.3 V, 0.4 V, 0.5 V and 1 V. The time-dependent EIS measurements of the cycled Li symmetric cells' resistance were conducted in the frequency range of 10^6 to 100 mHz with an amplitude of 10 mV. The distribution of specialized relaxation times in EIS spectra was analyzed using the DRT technique, implemented through a DRT Tool via MATLAB. CCD tests and galvanostatic discharge/charge tests of symmetric cells and full cells were conducted on the NEWARE battery test system (Shenzhen, China), within a voltage window of 2.8 to 4.3(4.7) V vs Li/Li⁺. All the above electrochemical tests were conducted at room temperature.

Supporting information

Supporting Information is available from the Wiley Online Library or from the author.

Acknowledgements

The authors would like to express their sincere thanks for the financial support from the Research Institute for Advanced Manufacturing (RIAM) (Project code: 1-CDJU), RCNN (Project No. 1-CE0H) of The Hong Kong Polytechnic University, National Natural Science Foundation of China (Grant Nos. W2441017, 22409103) and the "Innovation Yongjiang 2035" Key R&D Program (Grant Nos.2024Z040, 2025Z063).

Conflict of Interest

The authors declare no conflict of interest.

Data Availability Statement

The data that support the findings of this study are available from the corresponding author upon reasonable request.

Keywords

all-solid-state lithium batteries, argyrodite, lithium dendrites, artificial interlayer

Reference:

1. Li, J., et al., *Li metal anode interface in sulfide-based all-solid-state Li batteries*. EcoMat, 2023. **5**(8): p. e12383.
2. Janek, J. and W.G. Zeier, *Challenges in Speeding up Solid-State Battery Development*. Nature Energy, 2023. **8**(3): p. 230-240.
3. Nomura, Y. and K. Yamamoto, *Advanced Characterization Techniques for Sulfide-Based Solid-State Lithium Batteries*. Advanced Energy Materials, 2023. **13**(13): p. 2203883.
4. Dong, S., et al., *Challenges and Prospects of All-Solid-State Electrodes for Solid-State Lithium Batteries*. Advanced Functional Materials, 2023. **33**(49): p. 2304371.
5. Wang, J., et al., *Anode Interfacial Issues in Solid-State Li Batteries: Mechanistic Understanding and Mitigating Strategies*. Energy & Environmental Materials, 2023. **6**(4): p. e12613.
6. Ren, D., et al., *Challenges and opportunities of practical sulfide-based all-solid-state batteries*. Etransporation, 2023. **18**: p. 100272.
7. Jeong, S., et al., *Advances of sulfide-type solid-state batteries with negative electrodes: Progress and perspectives*. EcoMat, 2023. **5**(6): p. e12338.
8. Luo, S., et al., *Growth of lithium-indium dendrites in all-solid-state lithium-based batteries with sulfide electrolytes*. Nature Communications, 2021. **12**(1): p. 6968.
9. Narayanan, S., et al., *Effect of current density on the solid electrolyte interphase formation at the lithium⁺-Li₆PS₅Cl interface*. Nature Communications, 2022. **13**(1): p. 7237.
10. Zeng, D., et al., *Promoting favorable interfacial properties in lithium-based batteries using chlorine-rich sulfide inorganic solid-state electrolytes*. Nature Communications, 2022. **13**(1): p. 1909.
11. Hood, Z.D., et al., *Multifunctional Coatings on Sulfide-Based Solid Electrolyte Powders with Enhanced Processability, Stability, and Performance for Solid-State Batteries*. Advanced Materials, 2023. **35**(21): p. e2300673.
12. Liang, Z., et al., *Understanding the failure process of sulfide-based all-solid-state lithium batteries via operando nuclear magnetic resonance spectroscopy*. Nature Communications, 2023. **14**(1): p. 259.
13. Duan, H., et al., *In Situ Constructed 3D Lithium Anodes for Long-Cycling All-Solid-State Batteries*. Advanced Energy Materials, 2023. **13**(24): p. 2300815.
14. Kim, N., et al., *Carbide-mediated catalytic hydrogenolysis: defects in graphene on a carbonaceous lithium host for liquid and all-solid-state lithium metal batteries*. Energy & Environmental Science, 2023. **16**(6): p. 2505-2517.
15. Liang, Y., et al., *Tailoring Conversion-Reaction-Induced Alloy Interlayer for Dendrite-Free Sulfide-Based All-Solid-State Lithium-Metal Battery*. Advanced Science, 2023. **10**(19): p. 2300985.
16. Liu, C., et al., *Electron Redistribution Enables Redox-Resistible Li₆PS₅Cl towards High-Performance All-Solid-State Lithium Batteries*. Angewandte Chemie-international Edition, 2023. **62**(22): p. e202302655.
17. Shi, Y., et al., *An optimizing hybrid interface architecture for unleashing the potential of sulfide-based all-solid-state battery*. Energy Storage Materials, 2023. **63**: p. 103009.
18. Wan, H., et al., *Interface Design for High-Performance All-Solid-State Lithium Batteries*. Advanced Energy Materials, 2023. **14**(19): p. 2303046.

19. Wan, H., et al., *Interface design for all-solid-state lithium batteries*. Nature, 2023. **623**(7988): p. 739-744.
20. Wan, H., et al., *Critical interphase overpotential as a lithium dendrite-suppression criterion for all-solid-state lithium battery design*. Nature Energy, 2023. **8**(5): p. 473-481.
21. Lee, K., et al., *Multifunctional Interface for High-Rate and Long-Durable Garnet-Type Solid Electrolyte in Lithium Metal Batteries*. ACS Energy Letters, 2021. **7**(1): p. 381-389.
22. Ye, H., et al., *Guiding Uniform Li Plating/Stripping through Lithium-Aluminum Alloying Medium for Long-Life Li Metal Batteries*. Angewandte Chemie-international Edition, 2019. **58**(4): p. 1094-1099.
23. Krauskopf, T., et al., *Diffusion Limitation of Lithium Metal and Li-Mg Alloy Anodes on LLZO Type Solid Electrolytes as a Function of Temperature and Pressure*. Advanced Energy Materials, 2019. **9**(44): p. 1902568.
24. *Unlocking the in situ Li plating dynamics and evolution mediated by diverse metallic substrates in all-solid-state batteries*. Science Advances, 2022. **8**(43): p. eadd2000.
25. Chen, L., et al., *Reactive Magnesium Nitride Additive: A Drop-in Solution for Lithium/Garnet Wetting in All-Solid-State Batteries*. Angewandte Chemie-international Edition, 2023. **62**(27): p. e202305099.
26. Zhao, L., et al., *Imaging the evolution of lithium-solid electrolyte interface using operando scanning electron microscopy*. Nature Communications, 2025. **16**(1): p. 4283.
27. Wu, X., et al., *Developing High-Energy, Stable All-Solid-State Lithium Batteries Using Aluminum-Based Anodes and High-Nickel Cathodes*. Nanomicro Lett, 2025. **17**(1): p. 239.
28. Su, H., et al., *Localized Electrolyte Grain Engineering to Suppress Li Intrusion in All-Solid-State Batteries*. Advanced Materials, 2025. **37**(15): p. 2500673.
29. Avvaru, V.S., et al., *Tin-Carbon Dual Buffer Layer to Suppress Lithium Dendrite Growth in All-Solid-State Batteries*. ACS Nano, 2025. **19**(18): p. 17347-17356.
30. Zhu, J., et al., *A Porous Li-Al Alloy Anode toward High-Performance Sulfide-Based All-Solid-State Lithium Batteries*. Advanced Materials, 2024. **36**(39): p. 2407128.
31. Wang, Z.-X., et al., *Suppressing Li voids in all-solid-state lithium metal batteries through Li diffusion regulation*. Joule, 2024. **8**(10): p. 2794-2810.
32. Oh, J., et al., *All-Solid-State Batteries with Extremely Low N/P Ratio Operating at Low Stack Pressure*. Advanced Energy Materials, 2024. **15**(16): p. 2404817.
33. Su, H., et al., *A scalable Li-Al-Cl stratified structure for stable all-solid-state lithium metal batteries*. Nature Communications, 2024. **15**(1): p. 4202.
34. Wang, X., et al., *A Dynamically Stable Sulfide Electrolyte Architecture for High-Performance All-Solid-State Lithium Metal Batteries*. Small, 2023. **20**(22): p. 2306763.
35. Xu, S., et al., *Performance Enhancement of the Li₆PS₅Cl-Based Solid-State Batteries by Scavenging Lithium Dendrites with LaCl₃-Based Electrolyte*. Advanced Materials, 2024. **36**(15): p. 2310356.
36. Wang, C., et al., *In situ Triggered Rich-LiF/Mg Multifunctional Passivation Layer for Modifying the Anode Interface of All-Solid-State Lithium Metal Batteries*. Advanced Functional Materials, 2024. **35**(2): p. 2413176.
37. Zhang, N., et al., *Homogeneous Fluorine Doping toward Highly Conductive and Stable Li₁₀GeP₂S₁₂ Solid Electrolyte for All-Solid-State Lithium Batteries*. Advanced Materials, 2024. **36**(36): p. 2408903.

38. Liu, Y., et al., *Inhibiting Dendrites by Uniformizing Microstructure of Superionic Lithium Argyrodites for All-Solid-State Lithium Metal Batteries*. Advanced Energy Materials, 2024. **14**(31): p. 2400783.
39. Chen, Y., et al., *The Construction of Multifunctional Solid Electrolytes Interlayers for Stabilizing Li₆PS₅Cl-based All-Solid-State Lithium Metal Batteries*. Energy & Environmental Science, 2024. **17**(23): p. 9288-9302.
40. Li, H., et al., *A Cost-Effective Sulfide Solid Electrolyte Li₇P₃S_{7.5}O_{3.5} with Low Density and Excellent Anode Compatibility*. Angewandte Chemie-international Edition, 2024. **63**(37): p. e202407892.
41. Liu, Y., et al., *Ultrafast Synthesis of I-Rich Lithium Argyrodite Glass-Ceramic Electrolyte with High Ionic Conductivity*. Advanced Materials, 2022. **34**(3): p. e2107346.
42. Sandoval, S.E., et al., *Electro-chemo-mechanics of anode-free solid-state batteries*. Nature Materials, 2025. **24**(5): p. 673-681.
43. Ma, L., et al., *Current challenges and progress in anode/electrolyte interfaces of all-solid-state lithium batteries*. Etransportation, 2024. **20**: p. 100312.
44. Hu, X., et al., *External-pressure-electrochemistry coupling in solid-state lithium metal batteries*. Nature Reviews Materials, 2024. **9**(5): p. 305-320.
45. Zhang, J., et al., *Challenges and Strategies of Low-Pressure All-Solid-State Batteries*. Advanced Materials, 2024. **37**(6): p. 2413499.
46. Yu, T., et al., *Ductile Inorganic Solid Electrolytes for All-Solid-State Lithium Batteries*. Chemical Reviews, 2025. **125**(6): p. 3595-3662.
47. Wan, H., et al., *F and N Rich Solid Electrolyte for Stable All-Solid-State Battery*. Advanced Functional Materials, 2021. **32**(15): p. 2110876.
48. Xu, Y., et al., *Cross-Linked Polyamide-Integrated Argyrodite Li₆PS₅Cl for All-Solid-State Lithium Metal Batteries*. Small, 2025. **21**(3): p. e2408824.
49. Li, S., et al., *A Dynamically Stable Mixed Conducting Interphase for All-Solid-State Lithium Metal Batteries*. Advanced Materials, 2023. **36**(3): p. 2307768.
50. Zhang, S., et al., *Robust All-Solid-State Lithium Metal Batteries Enabled by a Composite Lithium Anode with Improved Bulk Li Diffusion Kinetics Properties*. ACS Nano, 2023. **17**(23): p. 24290-24298.
51. Lim, H., et al., *Rationally Designed Conversion-Type Lithium Metal Protective Layer for All-Solid-State Lithium Metal Batteries*. Advanced Energy Materials, 2024. **14**(12): p. 2303762.
52. Wei, C., et al., *SnF₂-Induced Multifunctional Interface-Stabilized Li_{5.5}PS_{4.5}Cl_{1.5}-Based All-Solid-State Lithium Metal Batteries*. Advanced Functional Materials, 2024. **34**(18): p. 2314306.
53. Shi, Y., et al., *A tailored dual-layer electronic shielding interface enables highly stable and dendrite-free solid-state lithium metal batteries*. Nano Energy, 2024. **120**: p. 109150.
54. Luo, M., et al., *Surface Coating Enabling Sulfide Solid Electrolytes with Excellent Air Stability and Lithium Compatibility*. Energy & Environmental Materials, 2024. **7**(6): p. e12753.
55. Li, D., et al., *A Versatile InF₃ Substituted Argyrodite Sulfide Electrolyte Toward Ultrathin Films for All-Solid-State Lithium Batteries*. Advanced Energy Materials, 2024. **14**(47): p. 2402929.
56. Lu, Y., et al., *The carrier transition from Li atoms to Li vacancies in solid-state lithium alloy anodes*. Science Advances, 2021. **7**(38): p. eabi5520.
57. Alt, C.D., et al., *Quantifying multiphase SEI growth in sulfide solid electrolytes*. Joule, 2024. **8**(10): p. 2755-2776.

58. Ji, X., et al., *Solid-State Electrolyte Design for Lithium Dendrite Suppression*. Advanced Materials, 2020. **32**(46): p. e2002741.
59. Ke, J., et al., *Metastability-Induced Atom Coordination and Electron Relocalization Toward Dendrite Free All-Solid-State Lithium Batteries*. Advanced Functional Materials, 2025. **35**(25): p. 2420170.
60. Ma, W., et al., *Regulated lithium deposition behavior by chlorinated hybrid solid-electrolyte-interphase for stable lithium metal anode*. Chemical Engineering Journal, 2022. **442**: p. 136297.
61. Hu, A., et al., *An artificial hybrid interphase for an ultrahigh-rate and practical lithium metal anode*. Energy & Environmental Science, 2021. **14**(7): p. 4115-4124.